RSC Advances

PAPER

View Article Online
View Journal | View Issue

Cite this: *RSC Adv.*, 2021, **11**, 12392

A three-dimensional flower-like NiCo-layered double hydroxide grown on nickel foam with an MXene coating for enhanced oxygen evolution reaction electrocatalysis†

Xuemei Li,[a] Zilu Zhang,[a] Qiankun Xiang,[a] Rongrong Chen,[a] Di Wu,[a] Guangyao Li[a] and Linjiang Wang *[abc]

Electrolysis of water is currently one of the cleanest and most efficient ways to produce high-purity hydrogen. The oxygen evolution reaction (OER) at the anode of electrolysis is the key factor affecting the reaction efficiency, which involves the transfer of four electrons and can slow down the overall reaction process. In this work, using nickel foam coated with MXene ($Ti_3C_2T_x$) as the carrier, a three-dimensional flower-shaped layered double hydroxide (NiCo-LDH) is grown on $Ti_3C_2T_x$ by a hydrothermal method to fabricate a NiCo-LDH/$Ti_3C_2T_x$/NF hybrid electrocatalyst for enhanced OER performance. The results reveal that the hybrid electrocatalyst has excellent OER activity in alkaline solution, in which a low overpotential of 223 mV and a small Tafel slope of 47.2 mV dec^{-1} can be achieved at a current density of 100 mA cm^{-2}. The interface interaction and charge transfer between $Ti_3C_2T_x$ and NiCo-LDH can accelerate the electron transfer rate during the redox process and improve the catalytic activity of the overall reaction. This NiCo-LDH/$Ti_3C_2T_x$/NF hybrid electrocatalyst may have important research significance and great application potential in catalytic electrolysis of water.

Received 19th February 2021
Accepted 15th March 2021

DOI: 10.1039/d1ra01368h

rsc.li/rsc-advances

Introduction

Hydrogen energy has attracted attention due to its high energy density and environmental friendliness as a result of aggravated environmental issues and the energy crisis.[1–4] Currently, electrolysis of water is an efficient approach to produce high-purity hydrogen. The electrolysis of water consists of the oxygen evolution reaction on the anode (OER, $2OH^- \rightarrow H_2O + 1/2O_2 + 2e^-$) and the hydrogen evolution reaction on the cathode (HER, $2H_2O + 2e^- \rightarrow H_2 + 2OH^-$). The OER involves the transfer of four electrons, which slows down the overall reaction rate, and thus it is desirable to develop an efficient OER catalyst to accelerate the reaction process.[5–7] Precious metals, such as Pt, Ru, Ir, and their oxides, are excellent OER catalysts but they suffer from high costs and shortages of resources. Therefore, it is still a huge challenge to develop efficient and inexpensive catalysts to replace precious metal catalysts.[8–10] At present, non-noble metal electrocatalysts, including carbides, nitride, oxides, sulfides, phosphates, alloys, oxides, hydroxides, and other active materials, are receiving extensive attention.[11–14] Layered double hydroxides (LDH), a typical kind of hydroxide, stand out among catalysts because of their advantages such as abundant active sites, low cost, simple preparation process, and modulation of composition and morphology.

Transition metal-based LDH were proven to have good OER catalytic activity under alkaline conditions in 2013. In recent years, Ni-based and Co-based LDH have proved to have excellent activity for the electrolysis of water.[15–19] However, the disadvantages of poor conductivity and a strong tendency to aggregate of LDH limit the electron conduction.[20] The fabrication of LDH with conductive carriers can overcome its poor conductivity, promote dispersion and expose more active sites of LDH.[21] Carbon materials, especially graphene with a large specific surface area, are often used as the carriers to promote dispersion and improve the electrical conductivity of LDH.[22–24] However, carbon materials have a low affinity for water and are difficult to firmly anchor on the metal precursors of LDH because of their non-polar surface.[25–27]

MXene ($M_{n+1}X_nT_x$) is a typical two-dimensional layered conductive material with a graphene-like structure, which can be obtained by selectively etching the A atoms from the MAX ($M_{n+1}AX_n$) phase.[28–31] MXene has attracted increasing attention due to its unique surface chemistry, adjustable composition,

[a]College of Materials Science and Engineering, Guilin University of Technology, Guilin 541004, China. E-mail: wlinjiang@163.com

[b]Key Laboratory of New Processing Technology for Nonferrous Metal & Materials, Ministry of Education, Guilin University of Technology, Guilin 541004, China

[c]Collaborative Innovation Center for Exploration of Nonferrous Metal Deposits and Efficient Utilization of Resources, Guilin University of Technology, Guilin 541004, China

† Electronic supplementary information (ESI) available. See DOI: 10.1039/d1ra01368h

physiochemical properties and high metal conductivity. Moreover, benefiting from the negatively charged layers of MXene and positively charged layers of LDH, the hybrid structure of LDH/MXene can have a strong interface interaction and electron coupling, which can expedite electronic transmission and enhance structural stability. Additionally, MXene can play a synergistic role in the OER process to accelerate the redox process of LDH.[32,33] Hao *et al.* reported a CoFe LDH/MXene electrocatalyst synthesized by *in situ* growth of CoFe LDH on MXene and the obtained catalyst exhibited a lower overpotential (319 mV) than CoFe LDH (352 mV) at the current density $j = 10$ mA cm^{-2}. Nevertheless, LDH/MXene OER electrocatalysts are always in the macroscopic state of a powder and they need to be coated on the electrode with adhesives such as Nafion or polyvinylidene fluoride, which restricts the contact between the active site and the electrolyte and reduces catalytic activity.[34–37]

Herein, using nickel foam (NF) and MXene ($Ti_3C_2T_x$) as the skeleton and the intermediate, a NiCo-LDH/$Ti_3C_2T_x$/NF hybrid structure is synthesized by a two-step method, where the $Ti_3C_2T_x$ coating layer on the NF skeleton is obtained by natural deposition firstly and then the three-dimensional flower-like NiCo-LDH is grown on the surface of $Ti_3C_2T_x$ by a hydrothermal method. The experimental results demonstrate that NF as the self-supporting electrode can promote the conductivity, while electronegative $Ti_3C_2T_x$ can be used as a binder to bind to positively charged LDH layers in the NiCo-LDH/$Ti_3C_2T_x$/NF hybrid structure. The interfacial interaction and electron transfer between NiCo-LDH and $Ti_3C_2T_x$ are of benefit. Furthermore, the three-dimensional flower-like structure of NiCo-LDH grown on a $Ti_3C_2T_x$/NF conductive substrate has a larger surface area, providing more effective edge sites. NiCo-LDH/$Ti_3C_2T_x$/NF had a low overpotential of 223 mV and a small Tafel slope of 47.2 mV dec^{-1} can be achieved at the current density $j = 100$ mA cm^{-2}. In a word, this hybrid catalyst can promote the advantages of NiCo-LDH, $Ti_3C_2T_x$ and NF in the electrocatalytic water splitting reaction and has a potential for broad prospective applications.

Materials and methods

Materials

$Ni(NO)_3 \cdot 6H_2O$, $Co(NO)_3 \cdot 6H_2O$, cetyl trimethylammonium chloride (CTAC), hydrochloric acid (HCl), hydrofluoric acid (HF), and acetone were obtained from Xilong Chemical Reagent Co., Ltd. MAX (Ti_3AlC_2) was purchased from Xinxi-technology Co., Ltd. Nickel foam (NF) was purchased from Changde Liyuan New Material Co., Ltd.

Synthesis of $Ti_3C_2T_x$

$Ti_3C_2T_x$ was synthesized according to the method in the literature. Typically, 0.5 g MAX (Ti_3AlC_2) was added into 30 ml HF solution and stirred for 24 h at room temperature to get a mixed solution. The mixed solution was centrifuged several times to remove the excess HF and dried under vacuum for 12 h at 60 °C to obtain $Ti_3C_2T_x$.

Synthesis of $Ti_3C_2T_x$/NF

0.2 g $Ti_3C_2T_x$ was added into 20 ml of deionized water and stirred evenly and then was treated with ultrasound 20 times at each ultrasonic time of 2 min in an ice bath to exfoliate $Ti_3C_2T_x$. Then the mixture was centrifuged at 3000 rpm for 30 min to remove the unpeeled $Ti_3C_2T_x$, and the exfoliated $Ti_3C_2T_x$ solution (denoted as d-$Ti_3C_2T_x$) was obtained.

Nickel foam (NF) was cut into pieces of 3 cm × 1.5 cm and then cleaned by ultrasound treatment with HCl solution (2.0 M) and acetone solution for 30 min, respectively. The cleaned NF was dried under vacuum at 60 °C for 2 h and then immersed in d-$Ti_3C_2T_x$ solution for 24 h to deposit d-$Ti_3C_2T_x$ on the surface of NF by electrostatic attraction. Then, it was dried under vacuum at 60 °C for 5 h and denoted $Ti_3C_2T_x$/NF.

Synthesis of NiCo-LDH/$Ti_3C_2T_x$/NF and NiCo-LDH/NF

0.77 g of $Ni(NO)_2 \cdot 6H_2O$, 0.38 g of $Co(NO)_2 \cdot 6H_2O$, 1.5 g of cetyl trimethylammonium chloride (CTAC), 50 ml of deionized water and 10 ml of methanol were added into an autoclave and mixed evenly, then $Ti_3C_2T_x$/NF was placed into the autoclave and reacted for 18 h at 180 °C to grow NiCo-LDH on the surface of $Ti_3C_2T_x$/NF and obtained NiCo-LDH/$Ti_3C_2T_x$/NF. When the reaction was completed, the NiCo-LDH/$Ti_3C_2T_x$/NF hybrid electrocatalyst was rinsed with deionized water and dried under vacuum at 60 °C for 5 h.

NiCo-LDH/NF was prepared by directly growing NiCo-LDH on a clean NF substrate under the same conditions.

Materials characterization

The crystalline structures of the electrocatalysts were analyzed by PAN Analytic X'Pert PRO X-ray diffraction (XRD) with a Cu-kα radiation source ($\lambda = 0.15405$ nm). Field-emission scanning electron microscopy (SEM, Hitachi S4800) and transmission electron microscopy (TEM, FEI Talos 200S) with elemental analysis was used to detect the microstructure and the composition of the electrocatalysts. Surface characteristics of the samples were investigated using a Thermo Scientific K-Alpha X-ray photoelectron spectrometer (XPS) and all peaks were calibrated using the standard C 1s (284.8 eV).

Electrocatalytic test

The OER catalytic performance of the electrocatalysts was evaluated using a standard CHI 660E electrochemical workstation with three electrodes. In 1.0 M KOH solution, a platinum plate was used as the counter electrode, saturated calomel electrode (SCE) as the reference electrode, and the NiCo-LDH/$Ti_3C_2T_x$/NF hybrid electrocatalyst was used as the working electrode. The measured potential was converted into a reversible hydrogen electrode according to the Nernst equation (E (*vs.* RHE) = E (*vs.* SCE) + 0.241 + 00.059pH). The electrocatalytic OER performance of the samples was evaluated by linear sweep voltammetry (LSV) with a scanning rate of 5 mV s^{-1} and a sampling interval of 1 mV, and the samples were compensated by 95% *iR* compensation. The electrochemical impedance spectroscopy (EIS) measured an amplitude of 5 mV, a frequency range of 1000 kHz–0.01 Hz, and a voltage of 0.5 V. The chronopotential measurement records do not include *iR* compensation.

Results and discussion

The synthetic strategy of the NiCo-LDH/$Ti_3C_2T_x$/NF hybrid electrocatalyst is shown in Fig. 1a. Before that, MXene ($Ti_3C_2T_x$) was synthesized by etching MAX (Ti_3AlC_2) in hydrofluoric acid (HF) (Fig. S1a†). A tightly packed lamellar structure of Ti_3AlC_2 could be detected from scanning electron microscope (SEM) images (Fig. S1b†), while the basal planes of $Ti_3C_2T_x$ fan out and spread apart as a result of the HF treatment (Fig. S1c†), which was attributed to the Al atom layer being replaced by T_x (*i.e.* OH and/or F). In contrast to Ti_3AlC_2, $Ti_3C_2T_x$ shows weakened diffraction peaks that can be indexed to the (002), (004), (104), and (105) signals of $Ti_3C_2T_x$ (Fig. S2†), which means its crystallinity decreased and the Al atom disappeared. Then, the multi-layered $Ti_3C_2T_x$ was further exfoliated to prepare d-$Ti_3C_2T_x$ with a foliated structure by ultrasonic treatment. The SEM images show that the surface of the NF skeleton was relatively uniform and smooth with many reticulated lines while more rough and obvious flakes could be seen on the NF skeleton surface after deposition of $Ti_3C_2T_x$ (Fig. S3†), which indicated that $Ti_3C_2T_x$ was successfully deposited on the NF surface. Benefiting from the electrostatic effect between $Ti_3C_2T_x$ and LDH, NiCo-LDH/$Ti_3C_2T_x$/NF was synthesized *via* a coating procedure of d-$Ti_3C_2T_x$ on the surface of the NF substrate followed by *in situ* growth of NiCo-LDH.[38] Based on the color change of the substrate in the photographs (Fig. S4†), it can also be speculated that the synthesis of the NiCo-LDH/$Ti_3C_2T_x$/NF hybrid electrocatalyst was successful. SEM analysis of NiCo-LDH/$Ti_3C_2T_x$/NF shows that the NiCo-LDH plates exhibited a three-dimensional (3D) flower-like structure with a diameter of about 10 μm (Fig. 1b). This 3D flower-like structure had the benefit of exposing the active sites in marginal areas and enhancing the catalytic activity based on the larger specific surface area.[39] The transmission electron microscopy (TEM) analysis was carried out to identify the microstructure of NiCo-LDH/$Ti_3C_2T_x$/NF and verified that NiCo-LDH and $Ti_3C_2T_x$ lamellae were stacked together due to electrostatic interaction, indicating the strong attraction between NiCo-LDH and $Ti_3C_2T_x$ (Fig. 1c). The high-resolution TEM analysis shows that the lattice fringe spacing was 0.25 nm, corresponding to the (012) plane of NiCo-LDH (Fig. 1d). The (012) and (110) crystal planes of the NiCo-LDH polycrystalline plate were calibrated by an electron diffraction pattern, which was consistent with the lattice fringe results. Element mapping analysis shows that Ni, Co, Ti, O, and C were uniformly distributed in the stripped NiCo-LDH/$Ti_3C_2T_x$/NF sample, indicating that NiCo-LDH grew uniformly on $Ti_3C_2T_x$ (Fig. 1e–j). In addition, NiCo-LDH with different morphologies can be obtained by adjusting the amount of Ni and Co nitrate precursors (Fig. S5†).

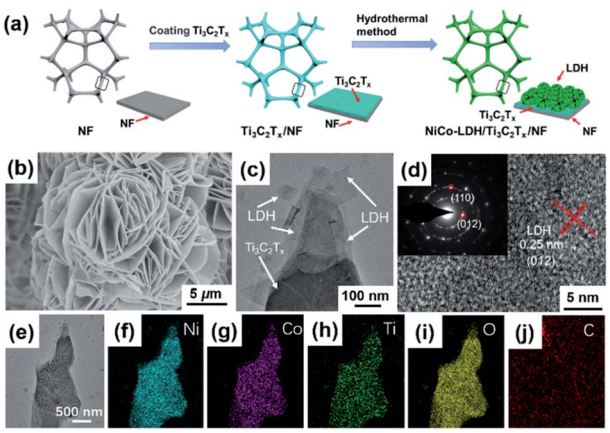

Fig. 1 (a) The preparation process of NiCo-LDH/$Ti_3C_2T_x$/NF, (b) SEM image of NiCo-LDH/$Ti_3C_2T_x$/NF, (c) TEM image of NiCo-LDH/$Ti_3C_2T_x$/NF, (d) HRTEM image and SAED pattern (inset) of NiCo-LDH/$Ti_3C_2T_x$/NF. (e–j) Elemental mapping showing the uniform distribution of Ni, Co, Ti, O, and C elements in NiCo-LDH/$Ti_3C_2T_x$/NF.

Due to its poor crystallinity, $Ti_3C_2T_x$, $Ti_3C_2T_x$/NF does not show a characteristic diffraction peak in the XRD pattern as compared to pure $Ti_3C_2T_x$ (Fig. 3a). After deposition of NiCo-LDH on $Ti_3C_2T_x$/NF, NiCo-LDH/$Ti_3C_2T_x$/NF had obvious diffraction peaks at around 11.8°, 23.2°, 35.3°, 39.6° and 46.6°, which correspond to the (003), (006), (009), (015), and (018) planes of LDH, indicating that NiCo-LDH had been successfully grown on the $Ti_3C_2T_x$/NF substrate. Furthermore, it can be seen that the diffraction peaks of NiCo-LDH in NiCo-LDH/$Ti_3C_2T_x$/NF were stronger than that in NiCo-LDH/NF, which may be because the hydroxyl group on the surface of $Ti_3C_2T_x$ had an adsorption capacity for Ni and Co cations, thus promoting the formation and growth of NiCo-LDH.

It was shown to contain chemical elements of Ni, Co, Ti, O, C, *etc.*, which was in accordance with the results of element mapping analysis. The Ti 2p spectrum of $Ti_3C_2T_x$/NF can be divided into four types of characteristic peaks, namely Ti–C (454.68 and 461.63 eV), Ti^{3+} (456.64 and 463.70 eV), Ti–O (458.78 and 464.53 eV) and Ti–F (460.39 and 465.44 eV) (Fig. S6a†), which proved that $Ti_3C_2T_x$ was deposited on the NF skeleton successfully.[40] However, the signal of the Ti 2p spectrum in NiCo-LDH/$Ti_3C_2T_x$/NF was concealed, which can be attributed to the high crystallization and thick lamellae of the growth of NiCo-LDH. This understanding can also be obtained by comparing the C 1s and O 1s spectra of $Ti_3C_2T_x$/NF, NiCo-LDH/$Ti_3C_2T_x$/NF, and NiCo-LDH/NF (Fig. S6†), which proved that $Ti_3C_2T_x$ existed as NiCo-LDH/$Ti_3C_2T_x$/NF. The standard peak of C 1s (284.8 eV) was used to calibrate the position of all the peaks before fitting and comparison. As clearly illustrated in Fig. 2c and d, the Ni^{3+}/Ni^{2+} and Co^{3+}/Co^{2+} area ratios increased in both the Ni 2p and Co 2p binding energy peaks of NiCo-LDH/$Ti_3C_2T_x$/NF compared to those of the NiCo-LDH/NF, indicating the strong interaction between NiCo-LDH and $Ti_3C_2T_x$. In addition, high-valence Ni and Co can regulate the electronic structure of LDH and were beneficial for the formation of NiOOH and CoOOH, which are the active substances in the process of water splitting electrolysis and can speed up OOH deprotonation to obtain O_2.[41–43]

The OER electrocatalytic performance of NiCo-LDH/$Ti_3C_2T_x$/NF was obtained using a standard three-electrode system in 1.0 M KOH solution. The NiCo-LDH/$Ti_3C_2T_x$/NF hybrid electrocatalyst was used as the working electrode and SCE and platinum plate were used as the reference and counter electrode, respectively (Fig. 3). It can be seen from Fig. 3a and b that

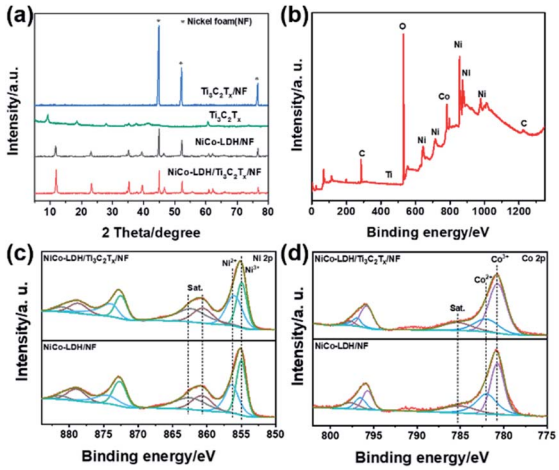

Fig. 2 (a) XRD patterns of NiCo-LDH/$Ti_3C_2T_x$/NF, NiCo-LDH/NF, $Ti_3C_2T_x$, and $Ti_3C_2T_x$/NF. (b) XPS spectra of NiCo-LDH/$Ti_3C_2T_x$/NF. (c and d) Ni 2p and Co 2p XPS spectra of NiCo-LDH/$Ti_3C_2T_x$/NF and NiCo-LDH/NF.

the catalytic activity of pure NF, IrO_2/NF, $Ti_3C_2T_x$/NF, and NiCo-LDH/NF was very weak with overpotentials of 494, 448, 389, and 331 mV at a current density of 100 mA cm^{-2}, respectively. On the other hand, the overpotential of NiCo-LDH/$Ti_3C_2T_x$/NF was 223 mV at the same current density, which was much lower than those of other electrocatalysts. This result implied that NiCo-LDH/$Ti_3C_2T_x$/NF shows a superior OER performance, which may be attributed to the synergistic effect of NiCo-LDH and $Ti_3C_2T_x$. The Tafel slopes of NiCo-LDH/$Ti_3C_2T_x$/NF (47.2 mV dec^{-1}) and NiCo-LDH/NF (52.7 mV dec^{-1}) shows in Fig. 3c indicate that NiCo-LDH/$Ti_3C_2T_x$/NF had kinetic advantages, which can be attributed to the reason that the presence of $Ti_3C_2T_x$ promotes electron transport, facilitates the chemical desorption process, accelerates the OOH- de-proton conversion to O_2, generates synergistic catalysis and improves the catalytic activity by means of the interface effect between $Ti_3C_2T_x$ and NiCo-LDH. NiCo-LDH/$Ti_3C_2T_x$/NF and NiCo-LDH/NF had double layer capacitance values of 8.58 and 5.25 mF cm^{-2}, indicating that NiCo-LDH-LDH/$Ti_3C_2T_x$/NF had a larger electrochemical active surface area, which can expose more active sites, and was more conducive to the release of catalyst active sites in the process of water splitting (Fig. 3d and S7†).

NiCo-LDH with different morphologies can be obtained by adjusting the amount of Ni and Co nitrate precursors. When the amounts of Ni and Co nitrate precursors were 0.8 mmol and 2.4 mmol, NiCo-LDH nanosheets grew vertically on the $Ti_3C_2T_x$/NF surface, which had double layer capacitance values of 3.51 and 5.86 mF cm^{-2} (Fig. 4c and S8†). When the Ni and Co amount was 4.0 mmol, NiCo-LDH was stacked into a 3D flower-like structure on the $Ti_3C_2T_x$/NF skeleton, it had the biggest double layer capacitance values of 8.58 mF cm^{-2} and the lowest overpotentials (Fig. 4). The overpotentials of NiCo-LDH/$Ti_3C_2T_x$/NF were 286, 254 and 223 mV at the current density of 100 mA cm^{-2} when the addition amount of Ni and Co nitrate precursor was 0.8 mmol, 2.4 mmol and 4.0 mmol, respectively. This was because flower-like NiCo-LDH may provide more effective edge sites, such as coordination steps, surface defects and corner atoms, and they were also the locations of the active sites.[44]

Electrochemical impedance spectroscopy (EIS) was utilized to investigate the charge transport properties of the electrocatalysts. In general, charge transfer resistance (R_{ct}) affects electrocatalytic kinetics and a lower R_{ct} value means a faster electron transfer rate. The radius of the half-circle corresponding to the charge transfer resistance (R_{ct}) of NiCo-LDH/$Ti_3C_2T_x$/NF was significantly smaller than that of NiCo-LDH/NF (Fig. 3e), which expressed that the presence of $Ti_3C_2T_x$ was conducive to accelerating the electron transfer between the catalyst and the conductive scaffold. For electrocatalysts, stability was also an important index. The voltage corresponding to j = 100 mA cm^{-2} was applied to NiCo-LDH/$Ti_3C_2T_x$/NF and NiCo-LDH/NF respectively, and the test was performed by chronopotentiometry. It could be seen that during the 12 h steady-state test, the I–t curve of NiCo-LDH/$Ti_3C_2T_x$/NF maintains a relatively stable state, while the curve of NiCo-LDH/NF shows a large fluctuation (Fig. 3f). In addition, the OER catalytic activity of NiCo-LDH/$Ti_3C_2T_x$/NF with a 3D flower-like structure obtained in this work was significantly superior to the IrO_2 commercial catalyst coated on NF (448 mV), and it is also in the forefront of the OER electrocatalysts reported in recent years (Table 1). As such, the NiCo-LDH/$Ti_3C_2T_x$/NF hybrid electrocatalyst shows superior OER

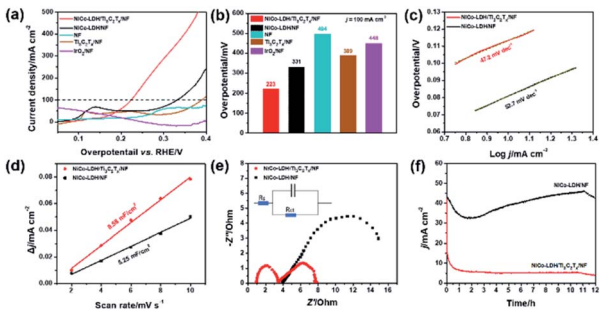

Fig. 3 (a) LSV curves of NiCo-LDH/$Ti_3C_2T_x$/NF, NiCo-LDH/NF, $Ti_3C_2T_x$/NF, NF, and IrO_2/NF. (b) Overpotentials of different catalysts at j = 100 mA cm^{-2}. (c) Tafel plots of NiCo-LDH/$Ti_3C_2T_x$/NF and NiCo-LDH/NF. (d) The corresponding charging current as a function of scan rate of NiCo-LDH/$Ti_3C_2T_x$/NF and NiCo-LDH/NF. (e) Electrochemical impedance spectroscopy Nyquist plots of NiCo-LDH/$Ti_3C_2T_x$/NF and NiCo-LDH/NF. (f) I–t curves of NiCo-LDH/$Ti_3C_2T_x$/NF and NiCo-LDH/NF.

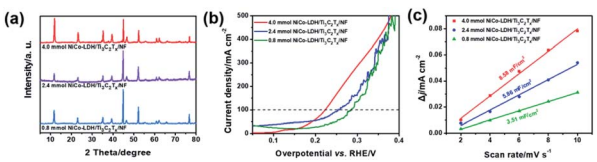

Fig. 4 (a) XRD patterns of NiCo-LDH/$Ti_3C_2T_x$/NF with different molar amounts of the Ni and Co nitrate precursors, (b) LSV curves and (c) the corresponding charging current as a function of the scan rate of NiCo-LDH/$Ti_3C_2T_x$/NF with different molar amounts of the Ni and Co nitrate precursors.

Table 1 OER catalysts that have been reported in recent years

Catalyst	Current density j (mA cm^{-2})	Overpotential η (mV)	Tafel slope (mV·dec^{-1})	Ref.
NiCo-LDH/$Ti_3C_2T_x$/NF	100	223	47.2	This work
NiFe-LDH/MXene	20	240	43	45
NiFe-LDH/NF	10	193	143.1	46
NiFe-LDH/MXene/NF	10	229	44	20
CoFe-LDH/MXene	10	319	50	34
NiFeCe-LDH/MXene	10	260	42.8	47
NiCo-LDH/MXene/NF	100	257.4	68	27
NiFeP-LDH/MXene	10	286	35	48
MXene/TiO_2/NiFeCo-LDH	10	320	98.4	49
NiFe LDH/NiTe/NF	50	228	51.04	50
NiFeAu LDH	100	267	58	51
CoP/MXene	10	280	95.4	26
Co_3O_4/MXene	10	300	118	52
$La_{0.8}Sr_{0.2}Co_{0.8}Fe_{0.2}O_{3-\delta}$	10	248	51	53
$Ni(OH)_2$@Ni/CC	100	458	168	54
FeCoNi alloy	10	400	70	55

activity and promising potential towards much broader energy related applications.

Conclusions

In summary, 3D flower-like NiCo-LDH was grown on a porous $Ti_3C_2T_x$/NF skeleton to fabricate a NiCo-LDH/$Ti_3C_2T_x$/NF hybrid electrocatalyst as a highly efficient OER electrocatalyst by a hydrothermal method for electrolysis of water. By combining the advantages of NiCo-LDH, $Ti_3C_2T_x$ and NF, the NiCo-LDH/$Ti_3C_2T_x$/NF hybrid electrocatalyst proved to have excellent OER activity in an alkaline environment. On the one hand, the interface interaction between $Ti_3C_2T_x$ and NiCo-LDH can effectively accelerate ion transfer, produce a synergistic effect and improve the OER catalytic activity. On the other hand, the 3D flower-like structure had a larger specific surface area and double layer capacitance values, which is conducive to the release of active sites. Compared with the OER catalysts with LDH/MXene hybrid structures reported in recent years, the 3D flower-like structure NiCo-LDH/$Ti_3C_2T_x$/NF had a better OER performance, a low overpotential of 223 mV and a small Tafel slope of 47.2 mV dec^{-1} could be achieved at a current density of 100 mA cm^{-2}. The new NiCo-LDH/$Ti_3C_2T_x$/NF hybrid electrocatalyst has broad application prospects in the field of electrolytic water splitting and this report provides a method to construct a ternary compound structure of NiCo-LDH, $Ti_3C_2T_x$ and a conductive frame.

Author contributions

Conceptualization, XL; methodology, XL and ZZ; software, XL; validation, XL and QX; formal analysis, XL; investigation, XL; resources, LW; data curation, XL and DW; writing – original draft preparation, XL; writing – review & editing, XL, QX, RC, GL, and LW; visualization, XL; supervision, LW; project administration, LW; and funding acquisition, LW. All authors have read and agreed to the published version of the manuscript.

Conflicts of interest

There are no conflicts to declare.

Acknowledgements

This work was supported by the National Natural Science Foundation of China (no. 42062003 and 41572034) and the Natural Science Foundation of Guangxi, China (no. 2018GXNSFAA294012).

References

1 E. Fabbri, A. Habereder, K. Waltar, R. Kötz and T. J. Schmidt, *Catal. Sci. Technol.*, 2014, **4**, 3800–3821.
2 I. Roger, M. A. Shipman and M. D. Symes, *Nat. Rev. Chem.*, 2017, **1**, 1–13.
3 S. Chu and A. Majumdar, *Nature*, 2012, **488**, 294–303.
4 B. Xiong, L. Chen and J. Shi, *ACS Catal.*, 2018, **8**, 3688–3707.
5 S. Anantharaj, K. Karthick and S. Kundu, *Mater. Today Energy*, 2017, **6**, 1–26.
6 C. Spori, J. T. H. Kwan, A. Bonakdarpour, D. P. Wilkinson and P. Strasser, *Angew. Chem., Int. Ed.*, 2017, **56**, 5994–6021.
7 Z. Sun, L. Lin, C. Nan, H. Li, G. Sun and X. Yang, *ACS Sustainable Chem. Eng.*, 2018, **6**, 14257–14263.
8 L. Deng, S. Jingying and L. Can, *Small*, 2018, **14**, 1704179.
9 T. Reier, M. Oezaslan and P. Strasser, *J. Am. Chem. Soc.*, 2012, **2**, 1765–1772.
10 Y. Lee, J. Suntivich, K. J. May, E. E. Perry and Y. Shao-Horn, *J. Phys. Chem. Lett.*, 2012, **3**, 399–404.
11 J. Zhang, X. Xie, C. Li, H. Wang and L. Wang, *RSC Adv.*, 2015, **5**, 29757–29765.
12 Z. Jian, Z. Qiuyu and F. Xinliang, *Adv. Mater.*, 2019, **31**, 1808167.
13 Y. Guo, T. Park, J. W. Yi, J. Henzie, J. Kim, Z. Wang, B. Jiang, Y. Bando, Y. Sugahara, J. Tang and Y. Yamauchi, *Adv. Mater.*, 2019, **31**, 1807134.

14 C. Hu and L. Dai, *Angew. Chem., Int. Ed.*, 2016, **55**, 11736–11758.
15 M. Gong, Y. Li, H. Wang, Y. Liang, J. Z. Wu, J. Zhou, T. Regier, F. Wei and H. Dai, *J. Phys. Chem. Lett.*, 2013, **135**, 8452–8455.
16 F. Yang, K. Sliozberg, I. Sinev, H. Antoni, A. Bähr, K. Ollegott, W. Xia, J. Masa, W. Grünert, B. R. Cuenya, W. Schuhmann and M. Muhler, *ChemSusChem*, 2017, **10**, 156–165.
17 Z. Lu, L. Qian, Y. Tian, Y. Li, X. Sun and X. Duan, *Chem. Commun.*, 2016, **52**, 908–911.
18 X. Ge, C. D. Gu, X. L. Wang and J. P. Tu, *J. Mater. Chem. A*, 2014, **2**, 17066–17076.
19 B. Chen, Z. Zhang, S. Kim, S. Lee, J. Lee, W. Kim and K. Yong, *ACS Appl. Mater. Interfaces*, 2018, **10**, 44518–44526.
20 N. Hao, Y. Wei, J. Wang, Z. Wang, Z. Zhu, S. Zhao, M. Han and X. Huang, *Nano Energy*, 2019, **63**, 103880.
21 S. Yin, W. Tu, Y. Sheng, Y. Du, M. Kraft, A. Borgna and R. Xu, *Adv. Mater.*, 2018, **30**, 1705106.
22 D. Zhou, Z. Cai, X. Lei, W. Tian, Y. Bi, Y. Jia, N. Han, T. Gao, Q. Zhang, Y. Kuang, J. Pan, X. Sun and X. Duan, *Adv. Energy Mater.*, 2018, **8**, 1701905.
23 W. Ma, R. Ma, J. Wu, P. Sun, X. Liu, K. Zhou and T. Sasaki, *Nanoscale*, 2016, **8**, 10425–10432.
24 D. H. Youn, Y. B. Park, J. Y. Kim, G. Magesh, Y. J. Jang and J. S. Lee, *J. Power Sources*, 2015, **294**, 437–443.
25 M. Yu, S. Zhou, Z. Wang, J. Zhao and J. Qiu, *Nano Energy*, 2018, **44**, 181–190.
26 L. Yan, B. Zhang, S. Wu and J. Yu, *J. Mater. Chem. A*, 2020, **8**, 14234–14242.
27 L. Hu, M. Li, X. Wei, H. Wang, Y. Wu, J. Wen, W. Gu and C. Zhu, *Chem. Eng. J.*, 2020, **398**, 125605.
28 M. Malaki, A. Maleki and R. S. Varma, *J. Mater. Chem. A*, 2019, **7**, 10843–10857.
29 H. Yu, Y. Wang, Y. Jing, J. Ma, C. Du and Q. Yan, *Small*, 2019, **15**, 1901503.
30 H. Niu, X. Yang, Q. Wang, X. Jing, K. Cheng, K. Zhu, K. Ye, G. Wang, D. Cao and J. Yan, *J. Energy Chem.*, 2020, **46**, 105–113.
31 S. Sun, C. Liao, A. M. Hafez, H. Zhu and S. Wu, *Chem. Eng. J.*, 2018, **338**, 27–45.
32 M. Benchakar, T. Bilyk, C. Garnero, L. Loupias, C. Morais, J. Pacaud, C. Canaff, P. Chartier, S. Morisset, N. Guignard, V. Mauchamp, S. Célérier and A. Habrioux, *Adv. Mater. Interfaces*, 2019, **6**, 1901328.
33 X. Dong, Y. Zhang, B. Ding, X. Hao, H. Dou and X. Zhang, *J. Power Sources*, 2018, **390**, 208–214.
34 C. Hao, Y. Wu, Y. An, B. Cui, J. Lin, X. Li, D. Wang, M. Jiang, Z. Cheng and S. Hu, *Mater. Today Energy*, 2019, **12**, 453–462.
35 F. Yan, D. Guo, J. Kang, L. Liu, C. Zhu, P. Gao, X. Zhang and Y. Chen, *Electrochim. Acta*, 2018, **283**, 755–763.
36 H. Yang, C. Wang, Y. Zhang and Q. Wang, *Sci. China Mater.*, 2018, **62**, 681–689.
37 R. Chen, G. Sun, C. Yang, L. Zhang, J. Miao, H. Tao, H. Yang, J. Chen, P. Chen and B. Liu, *Nanoscale Horiz.*, 2016, **1**, 156–160.
38 X. Zhan, C. Si, J. Zhou and Z. Sun, *Nanoscale Horiz.*, 2020, **5**, 235–258.
39 H. Zhong, T. Liu, S. Zhang, D. Li, P. Tang, N. Alonso-Vante and Y. Feng, *J. Energy Chem.*, 2019, **33**, 130–137.
40 X. Wu, B. Huang, Q. Wang and Y. Wang, *Chem. Eng. J.*, 2020, **380**, 122456.
41 Y. Bi, Z. Cai, D. Zhou, Y. Tian, Q. Zhang, Q. Zhang, Y. Kuang, Y. Li, X. Sun and X. Duan, *J. Catal.*, 2018, **358**, 100–107.
42 Y. Wang, S. Tao, H. Lin, S. Han, W. Zhong, Y. Xie, J. Hu and S. Yang, *RSC Adv.*, 2020, **10**, 33475–33482.
43 Q. Ma, B. Li, F. Huang, Q. Pang, Y. Chen and J. Zhang, *Electrochim. Acta*, 2019, **317**, 684–693.
44 K. Zhang, W. Wang, L. Kuai and B. Geng, *Electrochim. Acta*, 2017, **225**, 303–309.
45 X. Wang, Y. Lin, Y. Su, B. Zhang, C. Li, H. Wang and L. Wang, *Electrochim. Acta*, 2017, **225**, 263–271.
46 K. Huang, R. Dong, C. Wang, W. Li, H. Sun and B. Geng, *ACS Sustainable Chem. Eng.*, 2019, **7**, 15073–15079.
47 Y. Wen, Z. Wei, J. Liu, R. Li, P. Wang, B. Zhou, X. Zhang, J. Li and Z. Li, *J. Energy Chem.*, 2021, **52**, 412–420.
48 J. Chen, Q. Long, K. Xiao, T. Ouyang, N. Li, S. Ye and Z. Liu, *Sci. Bull.*, 2021, DOI: 10.1016/j.scib.2021.02.033.
49 N. Hao, Y. Wei, J. Wang, Z. Wang, Z. Zhu, S. Zhao, M. Han and X. Huang, *RSC Adv.*, 2018, **8**, 20576–20584.
50 H. Liuyong, X. Zeng, X. Wei, H. Wang, W. Yu, G. Wenling, S. Le and C. Zhu, *Appl. Catal., B*, 2020, **273**, 119014.
51 X. Li, W. Han, K. Xiao, T. Ouyang, N. Li, F. Peng and Z. Liu, *Catal. Sci. Technol.*, 2020, **10**, 4184–4190.
52 Y. Lu, D. Fan, Z. Chen, W. Xiao, C. Cao and X. Yang, *Sci. Bull.*, 2020, **65**, 460–466.
53 C. Zhao, N. Li, R. Zhang, Z. Zhu, J. Lin, K. Zhang and C. Zhao, *ACS Appl. Mater. Interfaces*, 2019, **11**, 47858–47867.
54 Z. Xing, L. Gan, J. Wang and X. Yang, *J. Mater. Chem. A*, 2017, **5**, 7744–7748.
55 S. Saha and A. K. Ganguli, *ChemistrySelect*, 2017, **2**, 1630–1636.